

ANCRe: Adaptive Neural Connection Reassignment for Efficient Depth Scaling

Yilang Zhang^{1,*}, Bingcong Li^{2,*}, Niao He², Georgios B. Giannakis¹

¹University of Minnesota, ²ETH Zurich

*Equal contribution.

Scaling network depth has been a central driver behind the success of modern foundation models, yet recent investigations suggest that deep layers are often underutilized. This paper revisits the default mechanism for deepening neural networks, namely residual connections, from an optimization perspective. Rigorous analysis proves that the layout of residual connections can fundamentally shape convergence behavior, and even induces an *exponential* gap in convergence rates. Prompted by this insight, we introduce adaptive neural connection reassignment (ANCRe), a principled and lightweight framework that parameterizes and learns residual connectivities from the data. ANCRe adaptively reassigns residual connections with negligible computational and memory overhead (< 1%), while enabling more effective utilization of network depth. Extensive numerical tests across pre-training of large language models, diffusion models, and deep ResNets demonstrate consistently accelerated convergence, boosted performance, and enhanced depth efficiency over conventional residual connections.

Emails: {zhan7453,georgios}@umn.edu, {bingcong.li,niao.he}@inf.ethz.ch

1 Introduction

Foundation models have demonstrated remarkable success across a broad spectrum of domains and impactful applications. For instance, large language models (LLMs) exhibit nearly human-level proficiency in various tasks, including conversational interaction (Achiam et al., 2023), automated code generation (Chen et al., 2021), and complex mathematical reasoning (Lewkowycz et al., 2022). Diffusion models have revolutionized vision tasks by enabling high-fidelity and controllable image synthesis (Ho et al., 2020; Song et al., 2021a,b). Recent work has further extended foundation models to multimodal settings, where joint representations are learned from heterogeneous data modalities (Radford et al., 2021; Driess et al., 2023).

One of the key factors underlying these advances is the increasing capacity of modern backbone architectures, with a particularly noticeable trend toward greater depth. For instance, the Llama 3.1 family employs 32, 80, and 126 Transformer layers for its 8B, 70B, and 405B variants, respectively (Grattafiori et al., 2024). Likewise, Diffusion Transformers (DiTs) scale in depth from 12 (DiT-S) up to 28 layers (DiT-XL) (Peebles and Xie, 2023). Moreover, (Csordás et al., 2025) shows a clear positive correlation between depth and performance across 132 open-source LLMs (see their Figure 1). This trend is also supported by theories. It is proved in (Telgarsky, 2015) that polynomially deep networks can express functions that would require exponential width in shallow ones.

Despite the documented success of deep networks, scaling model depth can be *less efficient* than it first appears. For example, (Csordás et al., 2025) shows that skipping an early layer in the Llama 3.1 70B has a remarkably greater impact on the outputs of subsequent layers than omitting a deep layer, and that deeper layers often behave as near-identity mappings. Since the identity

function is essentially available “for free”, this suggests that late layers are highly underutilized. Complementary evidence also occurs in multimodal foundation models, where the most informative vision embeddings are frequently found in intermediate layers of the Perception Encoder rather than the final layer (Bolya et al., 2025). Collectively, these observations reveal that the representational potential of depth is not fully exploited yet.

Given that residual (skip) connections are the default strategy and dominant mechanism for scaling model depth, this work revisits their design to enable more efficient depth scaling. Residual connections were proposed in (Srivastava et al., 2015; He et al., 2016a) to avoid vanishing and exploding gradients, and they have become almost universal across architectures. For example, the backbone architecture of LLMs, i.e., the Transformer (Vaswani et al., 2017), introduces residual connections around each self-attention and feedforward network modules. From an optimization perspective, residual connections are credited with smoothing the loss landscape, which facilitates training by improving the (local) condition number (Li et al., 2018).

This work continues on the optimization perspective of residual connections, and demonstrates an intuitive yet often overlooked factor: *where* residual connections are placed within a deep architecture, i.e., the residual *topology*, can play a crucial role in optimization. We provide quantitative theory showing that different topologies can induce an *exponential* gap in convergence for deep linear neural networks. This large gap motivates a principled redesign of residual layout. To this end, we term our approach adaptive neural connection reassignment (ANCRe¹), which learns an optimal residual topology from data. Our method not only achieves a linear convergence rate for deep linear networks, but also integrates seamlessly into modern architectures including LLMs, DiTs, and ResNets with consistent empirical gains. In a nutshell, our contributions are as follows:

- A theoretical characterization on the role of residual connection topology is established using deep linear neural networks, showing that different shortcut layouts can induce exponential gaps in convergence rates.
- ANCRe is proposed to parameterize residual connections and learn a data-driven topology on the fly via appropriately normalized shortcut coefficients. It incurs negligible computational and memory overhead.
- Extensive numerical evaluations are conducted under varying data modalities and network depths to systematically examine the efficiency of ANCRe. As an illustrative example, ANCRe achieves a $1.85\times$ training speedup on LLaMA-1B over conventional residual topology.

2 Related work

Residual connections. Residual (skip) connections are a primary mechanism for scaling neural networks to greater depth (Srivastava et al., 2015; He et al., 2016a,b). They were rapidly popularized in computer vision, with variants such as (Bachlechner et al., 2021) and DenseNet (Huang et al., 2017), and have since become a standard component of CNN-based architectures; see e.g., (Zagoruyko and Komodakis, 2016; Xie et al., 2017). In contrast, residual connections in large language models (LLMs) have remained relatively stable. Both Transformers and their recent variants adopt the same residual topology (Vaswani et al., 2017; Team et al., 2025; Touvron et al., 2023; Yang et al., 2025; Peebles and Xie, 2023), while certain shortcuts can be introduced to mitigate over-smoothing (Nguyen et al., 2023) or reduce KV cache size (Zhou et al., 2025). More recently, hyper-connections (HC) (Zhu et al., 2025) and manifold-constrained hyper-connections (mHC) (Xie et al., 2025) were proposed for

¹It coincides with “anchor” in French.

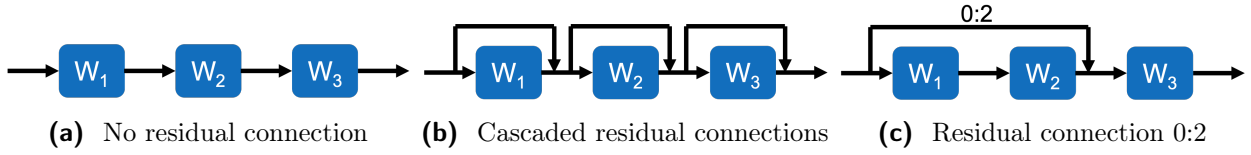


Figure 1 Visualization of linear neural network (LNN) of $K = 3$ layers.

foundation models as architectural alternatives. Our work is orthogonal to these lines of research: while they focus on intra-layer designs, we emphasize the *inter-layer topology*.

Understanding of residual connections. Residual connections are known to stabilize training by mitigating vanishing and exploding gradients (Haber and Ruthotto, 2017), and make gradients in deep networks less “shattered” (i.e., less like white noise) (Baldazzi et al., 2017). Empirical visualizations of ResNets also suggest that residual connections lead to a smoother loss landscape (Li et al., 2018). Theoretical understandings are often acquired by contrasting deep linear neural networks (Arora et al., 2019) with their residual counterparts. For example, the convergence of deep linear networks can degrade exponentially with depth (Shamir, 2019), whereas residual connections alleviate this slowdown (Wu et al., 2019). Moreover, residual connections can relax network width requirements for global converging in certain regimes, as by comparing results in (Du and Hu, 2019; Zou et al., 2020). The loss landscape of deep linear residual networks has also been studied in (Hardt and Ma, 2016). Our work enriches this line of results by showing that the *topology* of residual connections can affect convergence *exponentially*. More importantly, we translate this insight into a practical design that yields consistent improvements in modern architectures. Due to space limitation, other related work is deferred to Appendix A.

Notation. Bold lowercase (capital) letters denote vectors (matrices); $\|\cdot\|$ and $\|\cdot\|_F$ stand for ℓ_2 - and Frobenius-norm.

3 Residual topology matters: a case study

Popularized by ResNet (He et al., 2016a), residual connections allow each layer k to learn a residual mapping r_k relative to its input \mathbf{x}_k ; i.e., $g_k(\mathbf{x}_k) := r_k(\mathbf{x}_k) + \mathbf{x}_k$. By providing an identity shortcut, the loss landscape is more well-behaved (Li et al., 2018), thereby enabling training deep networks with hundreds of layers. This architecture has been extensively leveraged in foundation models (Vaswani et al., 2017; Wang et al., 2021; Radford et al., 2021) to train the network at scale. Residual connections are typically arranged in a cascaded structure as in Figure 1b, with each shortcut bypassing a single layer or block.

Despite the popularity of residual connections, their topology, i.e., the shortcut layout, is often fixed by default. This section revisits this simple design, and reveals a somewhat surprising message: in a theoretically convenient case study, *topology alone can provably induce exponentially different optimization behaviors*.

3.1 Linear neural networks with residual connections

Consider a commonly adopted prototype model, deep linear neural network (LNN), $f(\mathbf{x}) := \prod_{k=1}^K \mathbf{W}_k \mathbf{x} = \mathbf{W}_K \dots \mathbf{W}_2 \mathbf{W}_1 \mathbf{x}$ as sketched by Figure 1a, where $\mathbf{W}_k \in \mathbb{R}^{d \times d}$ denotes the learnable weights per layer k . This idealized model is often adopted for understanding the optimization and analyzing convergence of deep networks; see (Arora et al., 2019; Shamir, 2019) and more in

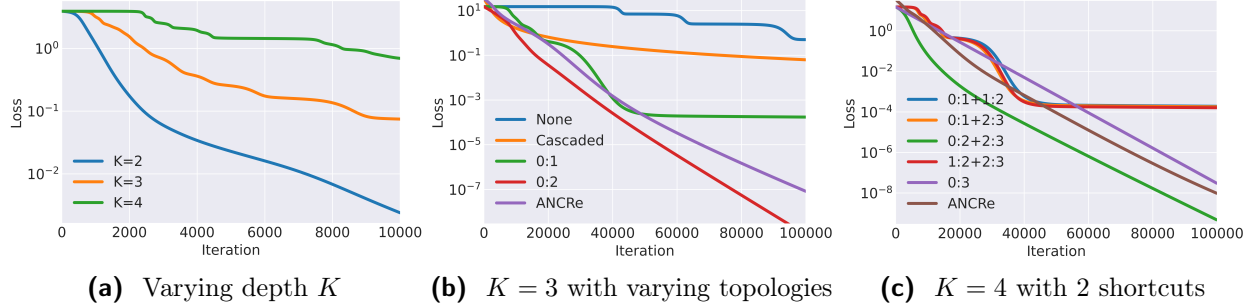


Figure 2 Convergence comparison of LNN under varying setups.

Section 2. In addition, consider also LNN augmented with residual connections. For brevity, we henceforth use $i:j$ to represent the shortcut bridging the outputs of layers i and j , where $0 \leq i < j \leq K$, and 0 represents the input of the first layer; see Figure 1c for an example.

Case Study 3.1. Given a K -layer LNN and input-output pair $\mathbf{X}, \mathbf{Y} \in \mathbb{R}^{d \times n}$ ($n \geq d$), define regression objective

$$\min_{\{\mathbf{W}_k\}_k} \mathcal{L}(\{\mathbf{W}_k\}_{k=1}^K) := \frac{1}{2} \left\| \prod_{k=1}^K \mathbf{W}_k \mathbf{X} - \mathbf{Y} \right\|_F^2.$$

Using standard gradient descent (GD) for training, Figure 2a outlines the loss evolution with depth $K = 2, 3, 4$, with vertical axis in log-scale. Without the aid of residual connection, the convergence slows down when the network grows deeper. Figure 2b depicts the convergence behavior of a 3-layer LNN under different residual connection topologies. While the conventional cascaded layout accelerates the convergence relative to no connection, it is not an optimal choice in this setup. In contrast, incorporating a single residual connection 0:1 or 0:2 yields remarkably faster convergence, where the latter further exhibits an exponential improvement over the former. Figure 2c extends the case study to a 4-layer LNN with 2 residual connections, and compares it with the optimal choice of a single connection 0:3. Notably, the model does not necessarily benefit from the additional residual connections, unless they are appropriately located.

Case Study 3.1 suggests that the configuration of residual connections can induce exponential discrepancies in convergence behaviors, and thus must be chosen cautiously. Nevertheless, there are currently neither rigorous theories supporting these observations, nor a principled approach for selecting an optimal topology. These two challenges call for an analytical investigation and numerical evaluations, which will be provided in the ensuing sections.

3.2 Convergence analysis of exponential discrepancies

This subsection establishes theories characterizing the exponentially different convergence behaviors induced by residual connections. To simplify the setup, our analysis considers the 3-layer LNN with a single residual connection (0:1 or 0:2), as illustrated in Figure 2b, while extension to nonlinear neural networks is left for future work. To eliminate the influence of step size, the analysis is performed under gradient flow (GF), the continuous-time counterpart of GD. Specifically, GF indexes the optimization time with a continuous variable $t \geq 0$, and updates the weight matrix through ordinary differential equation

$$\frac{d\mathbf{W}_k(t)}{dt} = -\nabla_{\mathbf{W}_k} \mathcal{L}(t), \quad k = 1, \dots, K \quad (1)$$

where the dependency of \mathcal{L} on $\{\mathbf{W}_k(t)\}_k$ is omitted for compactness. Clearly, GF can be viewed as an approximation of GD in the limit of infinitely small step sizes. Moreover, we assume the input data matrix \mathbf{X} is whitened, so that it's orthogonal; i.e., $\mathbf{X}\mathbf{X}^\top = \mathbf{I}_d$. This is a standard modeling choice that avoids unnecessarily over-complicating the analysis while still capturing the essential dynamics (Arora et al., 2019; Wu et al., 2019; Lion et al., 2025). When \mathbf{X} is a random matrix, this assumption corresponds to the data vectors being normalized and uncorrelated, which can be readily satisfied in practice without loss of generality.

Under these simplifications, the following two theorems establish respectively a lower bound for the LNN with the 0:1 shortcut, and an upper bound for the 0:2 one.

Theorem 3.2 (Lower bound). *Consider a 3-layer LNN with residual connection 0:1, and regression loss*

$$\mathcal{L}_1(t) := \frac{1}{2} \left\| \mathbf{W}_3(t) \mathbf{W}_2(t) (\mathbf{W}_1(t) + \mathbf{I}_d) \mathbf{X} - \mathbf{Y} \right\|_{\text{F}}^2. \quad (2)$$

For some sufficiently small initialization, GF in (1) cannot converge faster than a sublinear rate

$$\mathcal{L}_1(t) \geq \Omega(1/t^2). \quad (3)$$

Theorem 3.3 (Upper bound). *Consider a 3-layer LNN with residual connection 0:2, and regression loss*

$$\mathcal{L}_2(t) := \frac{1}{2} \left\| \mathbf{W}_3(t) (\mathbf{W}_2(t) \mathbf{W}_1(t) + \mathbf{I}_d) \mathbf{X} - \mathbf{Y} \right\|_{\text{F}}^2. \quad (4)$$

Under any sufficiently small initialization, GF in (1) ensures linear convergence

$$\mathcal{L}_2(t) \leq \mathcal{L}_2(0) e^{-2(1-\lambda)^2 t} \quad (5)$$

where $\lambda \in (0, 1)$ is a constant associated with the initialization $\{\mathbf{W}_k(0)\}_{k=1}^3$.

The formal statements of Theorems 3.2 and 3.3 involving all details can be found in Appendix B. We remark that small random initialization is standard in deep networks for numerical stability. While the 0:1 residual connection cannot be faster than a sublinear convergence rate, the 0:2 shortcut yields an exponential improvement. This corroborates our observation in Figure 2b, and validates that proper placements of residual connections can *exponentially* accelerate the training convergence. It is worth stressing that these results can be readily extended to $K > 3$; see Appendix B.4. To be specific, the 0:1 shortcut always corresponds to the slow case of sublinear convergence, whereas the $0:K-1$ one guarantees fast linear convergence. An example of the latter can be found in the 0:3 (violet) curve of Figure 2c.

Our case study and convergence analysis highlight *where* residual connections are placed could affect the convergence rate exponentially. This pronounced gap suggests that residual topology should be treated as a design lever for faster optimization. In the next section, we turn to the practical question of *how* to find a performant topology.

4 Learning residual connections from data

As observed in the previous section, even with the same network architecture, the residual topology pattern for fast convergence can change with depth (e.g., 0:2 for 3-layer and 1:2+2:3 for 4-layer LNNs in Figures 2b and 2c). More broadly, an optimal layout can depend on other architectural choices. It is thus difficult to prescribe a “panacea” of residual topology, especially for complex foundation models. This motivates learning the desirable topology on the fly.

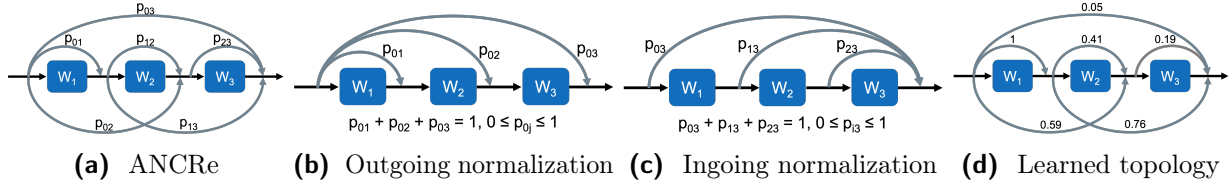


Figure 3 Visualization of ANCRe and two normalization schemes on a 3-layer LNN.

4.1 ANCRe: Adaptive neural connection reassignment

Instead of exhaustively searching over all the $2^{(L+1)L/2}$ possible topologies, our key idea is to parameterize the layout, and adaptively reassign the connectivity based on the network architecture and data distribution. Thus, we term our approach adaptive neural connection reassignment (ANCRe). In particular, ANCRe considers all possible shortcut connections $i:j$ ($i < j$), each associated with a coefficient p_{ij} that is optimized alongside the model parameters; cf. Figure 3a. We further probe two schemes for normalizing these weights, which we refer to as outgoing and ingoing normalizations, as exemplified in Figures 3b and 3c. This normalization ensures that the coefficients over candidate positions sum to 1. In particular, if some $p_{ij} = 1$, the construction reduces to adding a standard residual connection between layers i and j . As shown later in Section 5.4, this normalization is essential for stabilizing training at scale.

Outgoing normalization restricts the coefficients originating from layer i through a convex combination

$$\sum_{j=i+1}^K p_{ij} = 1, \quad 0 \leq p_{ij} \leq 1, \quad \forall 0 \leq i < j \leq K. \quad (6)$$

That says, the feature embedding from layer i is decomposed as $\mathbf{x}_i = \sum_{j=i+1}^K p_{ij} \mathbf{x}_i$, and each component is distributed to the subsequent layers. This ensures that the outgoing information per layer is bounded. Conversely, ingoing normalization imposes the following constraint

$$\sum_{i=0}^{j-1} p_{ij} = 1, \quad 0 \leq p_{ij} \leq 1, \quad \forall 0 \leq i < j \leq K \quad (7)$$

which preserves the input signal magnitude to layer j and enhances numerical stability. An alternative interpretation of this scheme is that it forms an *ensemble over network depths*. Letting $f_0(\mathbf{x}) := \mathbf{x}$ denote the initial input and $f_i(\mathbf{x})$ the output of layer i , the aggregated shortcuts to layer j incur $\sum_{i=0}^{j-1} p_{ij} f_i(\mathbf{x})$, which ensembles subnetworks of depths $0, \dots, j-1$, with p_{ij} serving as the routing coefficient.

In practice, both normalization constraints can be conveniently enforced via a softmax reparametrization. For example, the ingoing normalization can be formulated as

$$p_{ij} = \frac{\exp(c_{ij}/\tau)}{\sum_{k=1}^{j-1} \exp(c_{kj}/\tau)}, \quad \forall 0 \leq i < j \leq K \quad (8)$$

where $\tau > 0$ is a temperature hyperparameter, with a default value of 0.1 in practice. This softmax allows the model to emphasize beneficial shortcuts by driving $c_{ij} \rightarrow +\infty$, while suppressing detrimental ones with $c_{ij} \rightarrow -\infty$. Furthermore, if an effective configuration is known a priori, it can be readily incorporated through a regularizer. For instance, adding Tsallis entropy regularization (Tsallis, 1988) to the loss encourages sparse connectivity for softmax reparameterization. It is worth stressing that

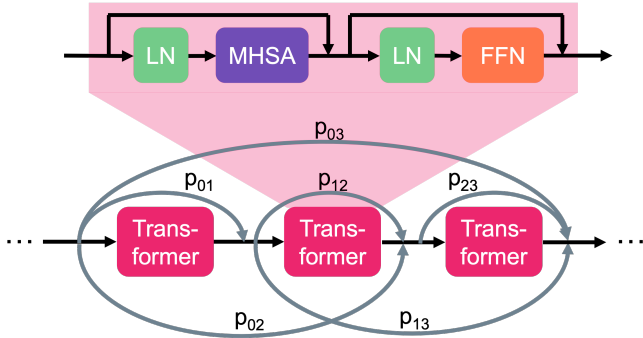


Figure 4 ANCRe applied to the standard Transformers comprising layer normalization (LN), multi-head self-attention (MHSA), and feedforward network (FFN) modules.

ANCRe introduces merely $K(K - 1)/2$ additional parameters c_{ij} , which is often fewer than a single feature dimension, and is negligible in modern deep networks. As a result, ANCRe preserves the highly desired computational efficiency; cf. Table 6.

While both normalizations work well in practice, we often find that ingoing normalization slightly outperforms the other at larger scale; see the ablation study in Section 5.4. We conjecture that this is due to the more stable input magnitude to each layer. For this reason, we stick to *ingoing normalization* (7) throughout the paper.

Regarding Case Study 3.1, ANCRe learns a data-driven connectivity, and hence achieves a linear convergence rate on par with the optimal case; cf. Figure 2b and 2c. The learned coefficients for the 3-layer LNN under ingoing normalization are visualized in Figure 3d, where certain shortcuts such as 0:3 and 2:3 are suppressed by the ingoing normalization. Aside from LNNs, the next subsection investigates how to effectively incorporate ANCRe into Transformers.

4.2 Applying ANCRe to Transformers

In modern Transformers, residual connections are applied separately to the multi-head self-attention (MHSA) and feedforward network (FFN) modules in a cascaded way, as illustrated in the upper part of Figure 4. We consider two granularities for placing ANCRe: module-level and block-level. The former introduces ANCRe connections from the input of the i -th FFN (resp. MHSA) to the input of the j -th FFN (resp. MHSA), while the latter bridges the inputs of entire Transformer blocks. Note that the block-level granularity coincides with the MHSA module-level one.

To determine the optimal granularity, a lightweight ablation study is performed by pre-training LLaMA-60M and LLaMA-130M (Touvron et al., 2023) on the C4 dataset (Raffel et al., 2020). As summarized in Table 1, establishing connectivity between MHSA inputs improves the validation perplexity (lower the better), whereas shortcuts originating from FFN inputs are less informative. Moreover, combining both connections yields performance comparable to using MHSA-only connections. For this reason, we adopt the MHSA-only (i.e. block-level) ANCRe for all subsequent tests involving Transformers; cf. Figure 4.

Next, tests are conducted on foundation models across multiple domains to showcase ANCRe’s effectiveness.

Table 1 Validation perplexity (\downarrow) by adding ANCRe to inputs of different modules.

MHSA	FFN	60M	130M
✗	✗	30.39	25.07
✓	✗	29.62	24.48
✗	✓	30.43	24.98
✓	✓	29.73	24.41

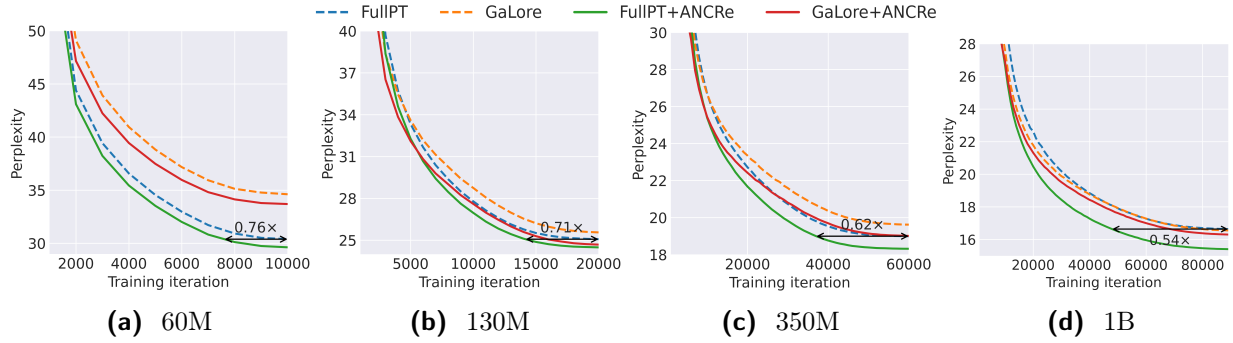


Figure 5 Validation perplexity evolution during pre-training of LLaMA models of different sizes.

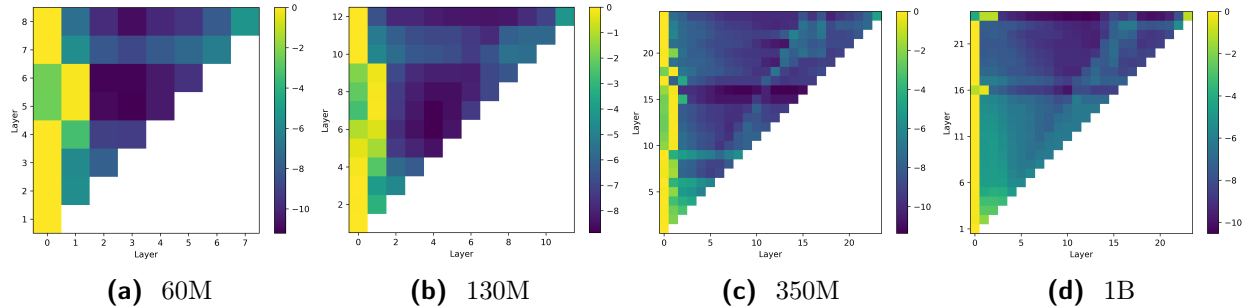


Figure 6 Visualization of residual coefficients $\log(c_{ij}/c_{\max,j})$ learned by ANCRe, where horizontal and vertical axes stand for i and j .

5 Numerical experiments

This section implements numerical tests to assess the performance of ANCRe, and compare it with vanilla cascaded residual connections (i.e., the standard architecture). All tests are conducted on servers with NVIDIA A100 and H100 GPUs. Additional setups including models, hyperparameters, and datasets are detailed in Appendix C.

5.1 Pre-training of LLMs

The evaluation of ANCRe begins with pre-training LLMs. Following the setups in (Lialin et al., 2024; Zhao et al., 2024), a series of LLaMA models (Touvron et al., 2023) are trained on the widely adopted C4 dataset (Raffel et al., 2020), which consists of cleaned English text collected across the Internet. The models span parameter counts of {60M, 130M, 350M, 1B}, with corresponding depths of {8, 12, 24, 24}. All experiments are run in BF16 precision. Two optimization schemes are considered: standard full pre-training (FullPT) and GaLore (Zhao et al., 2024), which applies low-rank gradient projection for memory efficiency. For both schemes, learning rates are selected from $\{5 \times 10^{-4}, 10^{-3}, 5 \times 10^{-3}, 10^{-2}, 5 \times 10^{-2}\}$. ANCRe directly adopts the learning rate optimized for cascaded residual connections without additional tuning.

Figure 5 plots the validation perplexity over pre-training iterations, while Table 2 reports quantitative results evaluated with the pre-trained models. Across all eight combinations of model sizes and optimization schemes, ANCRe consistently converges faster, and reduces perplexities by an average (\pm standard deviation) of 0.73 ± 0.33 . Notably, ANCRe matches the perplexity of cascaded residual connections using on average 34.3% fewer training iterations. The advantage grows from 24% to 46% as the network scales deeper. This underscores not only the significance of residual connection

Table 2 Perplexity (\downarrow) comparison of ANCRe and cascaded residual connections by pre-training LLaMA models of varying sizes. The better of the two are marked in solid lines.

Method	60M	130M	350M	1B
FullPT	30.39	25.07	19.00	16.64
FullPT+ANCRe	29.62	24.48	18.32	15.41
GaLore	34.61	25.56	19.62	16.55
GaLore+ANCRe	33.69	24.68	19.01	16.45
Training tokens	1.1B	2.2B	6.4B	13.1B

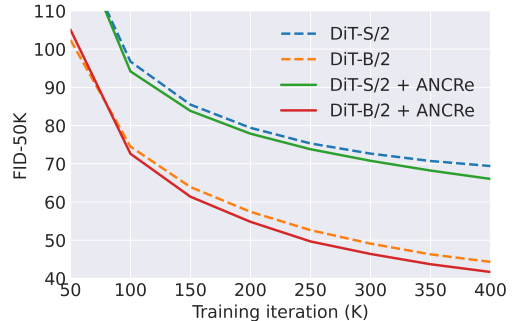


Figure 7 FID-50K evolution when pre-training DiT models.

Table 3 Comparison of ANCRe and cascaded residual connections by pre-training DiT models. The better of the two are marked in bold.

Model	FID \downarrow	sFID \downarrow	IS \uparrow	Precision \uparrow	Recall \uparrow
DiT-S/2	69.40	12.45	19.66	35.75%	55.82%
DiT-S/2+ANCRe	66.01	11.68	20.70	37.90%	57.80%
DiT-S/2 (cfg=1.5)	45.78	9.08	33.48	46.08%	54.25%
DiT-S/2+ANCRe (cfg=1.5)	42.99	8.61	35.04	48.53%	55.29%
DiT-B/2	44.31	8.42	32.89	47.93%	61.55%
DiT-B/2+ANCRe	41.66	7.89	34.40	50.42%	64.20%
DiT-B/2 (cfg=1.5)	22.41	6.35	65.27	60.75%	52.41%
DiT-B/2+ANCRe (cfg=1.5)	20.53	5.81	70.45	65.91%	56.51%

topology, but also the effectiveness of ANCRe in leveraging the increased depth.

In addition, Figure 6 sketches the residual coefficients learned by ANCRe. For clearer visualization, the heatmap is normalized by the largest ingoing coefficient $c_{\max,j} := \max_i c_{ij}$ per row j , and displayed on a logarithmic scale. Rather than relying solely on the shortcut from immediately preceding layer, deeper layers under ANCRe ensemble subnetworks of different depths. The learned connectivity patterns are also consistent across model sizes, with a predominant emphasis on shortcuts originating from the first two layers. Furthermore, larger models (350M and 1B) exhibit denser connectivity than the smaller ones, indicating more effective exploitation of network depth.

5.2 Pre-training of diffusion models

Beyond LLMs, pre-training of diffusion models is also inspected following the experimental protocols in Diffusion Transformers (DiT) (Peebles and Xie, 2023). Specifically, class-conditional latent DiT-S/2 and DiT-B/2 are trained on the ImageNet-1K dataset (Krizhevsky et al., 2012), which contains over 1.4 million images across 1,000 classes, at 256×256 resolution for 400,000 iterations. All hyperparameters including the learning rate are set to the defaults in (Peebles and Xie, 2023) without tuning. For evaluation, the standard Fréchet inception distance (FID) (Heusel et al., 2017) is calculated using 50,000 randomly sampled images from 250 DDPM steps (Ho et al., 2020), without classifier-free guidance (cfg) unless otherwise stated. Secondary metrics include spatial FID (sFID) (Nash et al., 2021), inception score (IS) (Salimans et al., 2016), and improved precision/recall (Kynkänniemi et al., 2019).

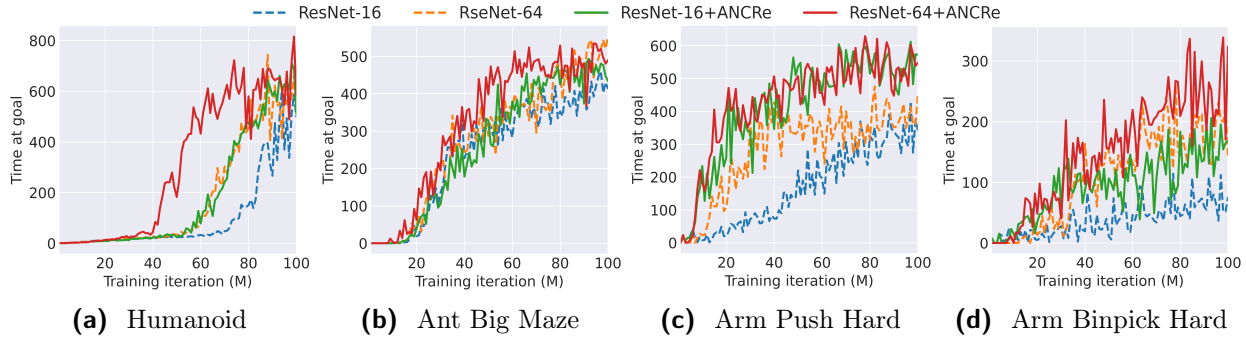


Figure 8 Reinforcement learning using ResNets of 16 and 64 layers.

The evolution of FID-50K over the pre-training iterations is outlined in Figure 7. It is observed that the incorporation of ANCRe remarkably accelerates the convergence, and leads to improved final performance, thanks to the effective utilization of network depth. It is worth noting that the performance gains are relatively smaller than those observed for LLMs, as DiT are generally shallower. In addition to the FID-50K, Table 3 reports auxiliary metrics computed using the pre-trained models for a more comprehensive comparison. Again, ANCRe consistently outperforms cascaded residual connections by an average of approximately 6% among metrics, demonstrating its effectiveness for different data modalities.

5.3 Reinforcement learning with ResNets

The third test examines reinforcement learning (RL) with “actions” as the modality. The test settings follow from (Wang et al., 2025), which demonstrates that scaling model depth in RL can unlock new goal-reaching capabilities. The test involves an unsupervised goal-conditioned regime, in which rewards are only available upon reaching the commanded goals. Broadly speaking, this setting follows the same spirit as RLVR (Lambert et al., 2024). Given that the sparse rewards provide rather limited feedback, the problem is considerably more challenging compared to standard RL scenarios supervised by dense rewards or expert demonstrations. Consequently, it necessitates deeper models of sufficient representational capacity. The models are ResNets (He et al., 2016a) of varying depths, with cascaded residual connections spanning consecutive blocks of four layers. ANCRe is applied at the same granularity of blocks, after removing the original cascaded residual connections. The RL benchmark encompasses four locomotion and manipulation tasks {Humanoid, Ant_Big_Maze, Arm_Push_Hard, Arm_Binpick_Hard} from the Gymnasium environments (Towers et al., 2025). Training is performed with the simple contrastive RL (CRL) algorithm (Eysenbach et al., 2022) for 100 million environment steps, and all hyperparameters are consistent with (Wang et al., 2025).

Figure 8 sketches the time-at-goal metric (\uparrow) averaged across episodes. For all four tasks, ANCRe consistently leads to considerably accelerated convergence than the vanilla ResNet baselines. Notably, when equipped with ANCRe, a 16-layer ResNet can match or even surpass the performance of a $4\times$ deeper ResNet. These results further corroborate that standard ResNet architectures tend to underutilize increased network depth, and demonstrate that ANCRe provides an effective plug-and-play remedy for improving depth efficiency.

5.4 Ablation study

The last group of numerical tests perform ablation studies to justify ANCRe’s design choices. The tests employ the setups as in Section 5.1 using the LLaMA-130M and LLaMA-350M models with

Table 4 Perplexity with different normalization schemes.

Normalization	130M	350M
None	diverge	diverge
Outgoing (6)	25.03	18.63
Ingoing (7)	24.48	18.32

Table 5 Ablation study using all or learnable shortcuts.

All $i:j$	Learnable	130M	350M
✓	✗	diverge	diverge
✗	✓	27.18	21.72
✓	✓	24.48	18.32

Table 6 Training time and GPU memory comparison.

Model, GPU, BS	ANCRe	Runtime	Memory
LLaMA-60M, 1×A100, 256	✗	6h55min	29.59GB
LLaMA-130M, 1×A100, 128	✗	14h45min	23.26GB
LLaMA-350M 4×A100, 64	✓	17h25min	27.21GB
	✓	17h32min	27.28GB

FullPT.

The first test compares the two normalization schemes discussed in Section 4.1. From Table 4, omitting normalization leads to divergence, since the coefficients can grow unbounded. It is further observed that ingoing normalization yields smaller fluctuations in the training loss and consequently achieves lower perplexity than outgoing normalization. This is because the former normalizes the inputs to each layer, so that computations are numerically stabler.

The second ablation study showcases that the effectiveness of ANCRe does not stem from simply adding more connections or making coefficients learnable. To see this, we consider two variants of ANCRe: one containing all possible shortcuts $i:j$ ($i < j$) but with constant coefficients $c_{ij} = 1/j$, and another with learnable cascaded residual connection on each Transformer block. As shown in Table 5, these variants either diverges or achieves less competitive performance. This highlights that ANCRe’s gains arise from the synergistic interaction between its connection topology and adaptive coefficient learning rather than either component alone.

Finally, we measure training runtime and GPU memory usage to assess the efficiency of ANCRe. As shown in Table 6, incorporating ANCRe introduces negligible computational and memory overhead across all model scales. In particular, the additional runtime remains within 1%, while the increase in peak GPU memory is consistently below 0.12GB. This efficiency arises because the forward and backward passes of the residual connections involve only a scalar–matrix multiplication and a matrix addition, which are ignorable compared to the dominant computations in Transformers. Together, these results demonstrate that ANCRe delivers performance gains with minimal overheads, ensuring its practical merits of extracting more performance from deep foundation models.

6 Conclusion and outlook

This paper investigated how the topology of residual connections fundamentally influences the convergence and depth efficiency of deep networks, and introduced adaptive neural connection reassignment (ANCRe) as a principled approach to learn the optimal residual connectivity. One

limitation of this work is that our analysis is limited to LNNs. Looking ahead, several directions have been added to the research agenda. First, to capture the optimization dynamics of nonlinear neural networks, the convergence analysis will be broadened to more general models beyond LNNs. Second, more effective schemes for parameterizing and normalizing residual connections tailored to foundation models such as Transformers will be explored, with an emphasis on improving stability and depth efficiency. Finally, pre-training tests will be scaled to larger models, for which efficient depth utilization becomes increasingly critical.

References

- Josh Achiam, Steven Adler, Sandhini Agarwal, Lama Ahmad, Ilge Akkaya, Florencia Leoni Aleman, Diogo Almeida, Janko Altenschmidt, Sam Altman, Shyamal Anadkat, et al. Gpt-4 technical report. *arXiv preprint arXiv:2303.08774*, 2023.
- Sanjeev Arora, Nadav Cohen, Noah Golowich, and Wei Hu. A convergence analysis of gradient descent for deep linear neural networks. In *Proc. Int. Conf. on Learning Representations (ICLR)*, 2019.
- Thomas Bachlechner, Bodhisattwa Prasad Majumder, Henry Mao, Gary Cottrell, and Julian McAuley. ReZero is all you need: fast convergence at large depth. In *Proc. Conf. on Uncertainty in Artificial Intelligence (UAI)*, volume 161, pages 1352–1361, 27–30 Jul 2021.
- David Balduzzi, Marcus Frean, Lennox Leary, JP Lewis, Kurt Wan-Duo Ma, and Brian McWilliams. The shattered gradients problem: If resnets are the answer, then what is the question? In *Proc. Int. Conf. on Machine Learning (ICML)*, pages 342–350, 2017.
- Daniel Bolya, Po-Yao Huang, Peize Sun, Jang Hyun Cho, Andrea Madotto, Chen Wei, Tengyu Ma, Jiale Zhi, Jathushan Rajasegaran, Hanoona Rasheed, et al. Perception encoder: The best visual embeddings are not at the output of the network. *arXiv preprint arXiv:2504.13181*, 2025.
- Mark Chen, Jerry Tworek, Heewoo Jun, Qiming Yuan, Henrique Ponde De Oliveira Pinto, Jared Kaplan, Harri Edwards, Yuri Burda, Nicholas Joseph, Greg Brockman, et al. Evaluating large language models trained on code. *arXiv preprint arXiv:2107.03374*, 2021.
- Róbert Csordás, Christopher D Manning, and Christopher Potts. Do language models use their depth efficiently? *arXiv preprint arXiv:2505.13898*, 2025.
- Soham De and Sam Smith. Batch normalization biases residual blocks towards the identity function in deep networks. *Proc. Neural Information Processing Systems (NeurIPS)*, 33:19964–19975, 2020.
- Danny Driess, Fei Xia, Mehdi S. M. Sajjadi, Corey Lynch, Aakanksha Chowdhery, Brian Ichter, Ayzaan Wahid, Jonathan Tompson, Quan Vuong, Tianhe Yu, Wenlong Huang, Yevgen Chebotar, Pierre Sermanet, Daniel Duckworth, Sergey Levine, Vincent Vanhoucke, Karol Hausman, Marc Toussaint, Klaus Greff, Andy Zeng, Igor Mordatch, and Pete Florence. PaLM-e: An embodied multimodal language model. In *Proc. Int. Conf. on Machine Learning (ICML)*, volume 202, pages 8469–8488, 23–29 Jul 2023.
- Simon Du and Wei Hu. Width provably matters in optimization for deep linear neural networks. In *Proc. Int. Conf. on Machine Learning (ICML)*, pages 1655–1664, 2019.
- Benjamin Eysenbach, Tianjun Zhang, Sergey Levine, and Russ R Salakhutdinov. Contrastive learning as goal-conditioned reinforcement learning. In *Proc. Neural Information Processing Systems (NeurIPS)*, volume 35, pages 35603–35620, 2022.
- Aaron Grattafiori, Abhimanyu Dubey, Abhinav Jauhri, Abhinav Pandey, Abhishek Kadian, Ahmad Al-Dahle, Aiesha Letman, Akhil Mathur, Alan Schelten, Alex Vaughan, et al. The llama 3 herd of models. *arXiv preprint arXiv:2407.21783*, 2024.
- Eldad Haber and Lars Ruthotto. Stable architectures for deep neural networks. *Inverse problems*, 34(1):014004, 2017.

- Moritz Hardt and Tengyu Ma. Identity matters in deep learning. *arXiv preprint arXiv:1611.04231*, 2016.
- Kaiming He, Xiangyu Zhang, Shaoqing Ren, and Jian Sun. Deep residual learning for image recognition. In *Proc. Conf. Computer Vision and Pattern Recognition (CVPR)*, June 2016a.
- Kaiming He, Xiangyu Zhang, Shaoqing Ren, and Jian Sun. Identity mappings in deep residual networks. In *Proc. European Conf. on Computer Vision (ECCV)*, pages 630–645. Springer, 2016b.
- Martin Heusel, Hubert Ramsauer, Thomas Unterthiner, Bernhard Nessler, and Sepp Hochreiter. GANs trained by a two time-scale update rule converge to a local nash equilibrium. In *Proc. Neural Information Processing Systems (NeurIPS)*, volume 30, 2017.
- Jonathan Ho, Ajay Jain, and Pieter Abbeel. Denoising diffusion probabilistic models. In *Advances in Neural Information Processing Systems*, volume 33, pages 6840–6851, 2020.
- Edward Hu, Yelong Shen, Phillip Wallis, Zeyuan Allen-Zhu, Yuanzhi Li, Shean Wang, Lu Wang, and Weizhu Chen. LoRA: Low-rank adaptation of large language models. In *Proc. Int. Conf. on Learning Representations (ICLR)*, 2022.
- Gao Huang, Zhuang Liu, Laurens Van Der Maaten, and Kilian Q Weinberger. Densely connected convolutional networks. In *Proc. Conf. Computer Vision and Pattern Recognition (CVPR)*, pages 4700–4708, 2017.
- Alex Krizhevsky, Ilya Sutskever, and Geoffrey E Hinton. Imagenet classification with deep convolutional neural networks. In *Proc. Neural Information Processing Systems (NeurIPS)*, volume 25, 2012.
- Tuomas Kynkänniemi, Tero Karras, Samuli Laine, Jaakko Lehtinen, and Timo Aila. Improved precision and recall metric for assessing generative models. In *Proc. Neural Information Processing Systems (NeurIPS)*, volume 32, 2019.
- Nathan Lambert, Jacob Morrison, Valentina Pyatkin, Shengyi Huang, Hamish Ivison, Faeze Brahman, Lester James V Miranda, Alisa Liu, Nouha Dziri, Shane Lyu, et al. Tulu 3: Pushing frontiers in open language model post-training. *arXiv preprint arXiv:2411.15124*, 2024.
- Aitor Lewkowycz, Anders Andreassen, David Dohan, Ethan Dyer, Henryk Michalewski, Vinay Ramasesh, Ambrose Slone, Cem Anil, Imanol Schlag, Theo Gutman-Solo, Yuhuai Wu, Behnam Neyshabur, Guy Gur-Ari, and Vedant Misra. Solving quantitative reasoning problems with language models. In *Proc. Neural Information Processing Systems (NeurIPS)*, volume 35, pages 3843–3857, 2022.
- Bingcong Li, Liang Zhang, Aryan Mokhtari, and Niao He. On the crucial role of initialization for matrix factorization. *arXiv preprint arXiv:2410.18965*, 2024.
- Hao Li, Zheng Xu, Gavin Taylor, Christoph Studer, and Tom Goldstein. Visualizing the loss landscape of neural nets. *Proc. Neural Information Processing Systems (NeurIPS)*, 31, 2018.
- Vladislav Lalin, Sherin Muckatira, Namrata Shivagunde, and Anna Rumshisky. ReLoRA: High-rank training through low-rank updates. In *Proc. Int. Conf. on Learning Representations (ICLR)*, 2024.
- Kai Lion, Liang Zhang, Bingcong Li, and Niao He. Polar: Polar-decomposed low-rank adapter representation. In *Proc. Neural Information Processing Systems (NeurIPS)*, 2025.
- Ilya Loshchilov and Frank Hutter. Decoupled weight decay regularization. In *Proc. Int. Conf. on Learning Representations (ICLR)*, 2017.
- Charlie Nash, Jacob Menick, Sander Dieleman, and Peter Battaglia. Generating images with sparse representations. In *Proc. Int. Conf. on Machine Learning (ICML)*, volume 139, pages 7958–7968, 18–24 Jul 2021.
- Tam Nguyen, Tan Nguyen, and Richard Baraniuk. Mitigating over-smoothing in transformers via regularized nonlocal functionals. In *Proc. Neural Information Processing Systems (NeurIPS)*, volume 36, pages 80233–80256, 2023.

William Peebles and Saining Xie. Scalable diffusion models with transformers. In *Proc. Int. Conf. on Computer Vision (ICCV)*, pages 4195–4205, October 2023.

Alec Radford, Jong Wook Kim, Chris Hallacy, Aditya Ramesh, Gabriel Goh, Sandhini Agarwal, Girish Sastry, Amanda Askell, Pamela Mishkin, Jack Clark, Gretchen Krueger, and Ilya Sutskever. Learning transferable visual models from natural language supervision. In *Proc. Int. Conf. on Machine Learning (ICML)*, volume 139, pages 8748–8763, 18–24 Jul 2021.

Colin Raffel, Noam Shazeer, Adam Roberts, Katherine Lee, Sharan Narang, Michael Matena, Yanqi Zhou, Wei Li, and Peter J. Liu. Exploring the limits of transfer learning with a unified text-to-text transformer. *J. Mach. Learn. Res.*, 21(140):1–67, 2020.

Tim Salimans, Ian Goodfellow, Wojciech Zaremba, Vicki Cheung, Alec Radford, Xi Chen, and Xi Chen. Improved techniques for training gans. In *Proc. Neural Information Processing Systems (NeurIPS)*, volume 29, 2016.

Ohad Shamir. Exponential convergence time of gradient descent for one-dimensional deep linear neural networks. In *Proc. Annual Conf. on Learning Theory (COLT)*, volume 99, pages 2691–2713, 25–28 Jun 2019.

Jiaming Song, Chenlin Meng, and Stefano Ermon. Denoising diffusion implicit models. In *Proc. Int. Conf. on Learning Representations (ICLR)*, 2021a.

Yang Song, Jascha Sohl-Dickstein, Diederik P Kingma, Abhishek Kumar, Stefano Ermon, and Ben Poole. Score-based generative modeling through stochastic differential equations. In *Proc. Int. Conf. on Learning Representations (ICLR)*, 2021b.

Rupesh Kumar Srivastava, Klaus Greff, and Jürgen Schmidhuber. Highway networks. *arXiv preprint arXiv:1505.00387*, 2015.

Gemma Team, Aishwarya Kamath, Johan Ferret, Shreya Pathak, Nino Vieillard, Ramona Merhej, Sarah Perrin, Tatiana Matejovicova, Alexandre Ramé, Morgane Rivière, et al. Gemma 3 technical report. *arXiv preprint arXiv:2503.19786*, 2025.

Matus Telgarsky. Representation benefits of deep feedforward networks. *arXiv preprint arXiv:1509.08101*, 2015.

Hugo Touvron, Matthieu Cord, Alexandre Sablayrolles, Gabriel Synnaeve, and Hervé Jégou. Going deeper with image transformers. In *Proc. Int. Conf. on Computer Vision (ICCV)*, pages 32–42, 2021.

Hugo Touvron, Thibaut Lavril, Gautier Izacard, Xavier Martinet, Marie-Anne Lachaux, Timothée Lacroix, Baptiste Rozière, Naman Goyal, Eric Hambro, Faisal Azhar, et al. Llama: Open and efficient foundation language models. *arXiv preprint arXiv:2302.13971*, 2023.

Mark Towers, Ariel Kwiatkowski, John U. Balis, Gianluca De Cola, Tristan Deleu, Manuel Goulão, Kallinteris Andreas, Markus Krimmel, Arjun KG, Rodrigo De Lazcano Perez-Vicente, J K Terry, Andrea Pierré, Sander V Schulhoff, Jun Jet Tai, Hannah Tan, and Omar G. Younis. Gymnasium: A standard interface for reinforcement learning environments. In *The Thirty-ninth Annual Conference on Neural Information Processing Systems Datasets and Benchmarks Track*, 2025.

Constantino Tsallis. Possible generalization of boltzmann-gibbs statistics. *Journal of statistical physics*, 52(1): 479–487, 1988.

Ashish Vaswani, Noam Shazeer, Niki Parmar, Jakob Uszkoreit, Llion Jones, Aidan N Gomez, Łukasz Kaiser, and Illia Polosukhin. Attention is all you need. In *Proc. Neural Information Processing Systems (NeurIPS)*, volume 30, 2017.

Hongyu Wang, Shuming Ma, Li Dong, Shaohan Huang, Dongdong Zhang, and Furu Wei. DeepNet: Scaling transformers to 1,000 layers. *IEEE Trans. Pattern Anal. Mach. Intel.*, 46(10):6761–6774, 2024a.

- Kevin Wang, Ishaan Javali, Michał Bortkiewicz, Tomasz Trzcinski, and Benjamin Eysenbach. 1000 layer networks for self-supervised RL: Scaling depth can enable new goal-reaching capabilities. In *Proc. Neural Information Processing Systems (NeurIPS)*, 2025.
- Yulin Wang, Rui Huang, Shiji Song, Zeyi Huang, and Gao Huang. Not all images are worth 16x16 words: Dynamic transformers for efficient image recognition. In *Proc. Neural Information Processing Systems (NeurIPS)*, volume 34, pages 11960–11973, 2021.
- Zhengbo Wang, Jian Liang, Ran He, Zilei Wang, and Tieniu Tan. Lora-pro: Are low-rank adapters properly optimized? *arXiv preprint arXiv:2407.18242*, 2024b.
- Lei Wu, Qingcan Wang, and Chao Ma. Global convergence of gradient descent for deep linear residual networks. *Proc. Neural Information Processing Systems (NeurIPS)*, 32, 2019.
- Saining Xie, Ross Girshick, Piotr Dollár, Zhuowen Tu, and Kaiming He. Aggregated residual transformations for deep neural networks. In *Proc. Conf. Computer Vision and Pattern Recognition (CVPR)*, pages 1492–1500, 2017.
- Zhenda Xie, Yixuan Wei, Huanqi Cao, Chenggang Zhao, Chengqi Deng, Jiashi Li, Damai Dai, Huazuo Gao, Jiang Chang, Liang Zhao, et al. mhc: Manifold-constrained hyper-connections. *arXiv preprint arXiv:2512.24880*, 2025.
- Ruixin Xiong, Yunchang Yang, Di He, Kai Zheng, Shuxin Zheng, Chen Xing, Huishuai Zhang, Yanyan Lan, Liwei Wang, and Tieyan Liu. On layer normalization in the transformer architecture. In *Proc. Int. Conf. on Machine Learning (ICML)*, volume 119, pages 10524–10533, 13–18 Jul 2020.
- An Yang, Anfeng Li, Baosong Yang, Beichen Zhang, Binyuan Hui, Bo Zheng, Bowen Yu, Chang Gao, Chengan Huang, Chenxu Lv, et al. Qwen3 technical report. *arXiv preprint arXiv:2505.09388*, 2025.
- Sergey Zagoruyko and Nikos Komodakis. Wide residual networks. *arXiv preprint arXiv:1605.07146*, 2016.
- Hongyi Zhang, Yann N Dauphin, and Tengyu Ma. Fixup initialization: Residual learning without normalization. *arXiv preprint arXiv:1901.09321*, 2019.
- Yilang Zhang, Bingcong Li, and Georgios B Giannakis. Reflora: Refactored low-rank adaptation for efficient fine-tuning of large models. *arXiv preprint arXiv:2505.18877*, 2025.
- Jiawei Zhao, Zhenyu Zhang, Beidi Chen, Zhangyang Wang, Anima Anandkumar, and Yuandong Tian. GaLore: Memory-efficient LLM training by gradient low-rank projection. In *Proc. Int. Conf. on Machine Learning (ICML)*, volume 235 of *Proceedings of Machine Learning Research*, pages 61121–61143, 21–27 Jul 2024.
- Zhanchao Zhou, Tianyi Wu, Zhiyun Jiang, Fares Obeid, and Zhenzhong Lan. Value residual learning. In *Proc. Conf. Assoc. Comput. Linguist. Meet. (ACL)*, pages 28341–28356, July 2025.
- Defa Zhu, Hongzhi Huang, Zihao Huang, Yutao Zeng, Yunyao Mao, Banggu Wu, Qiyang Min, and Xun Zhou. Hyper-connections. In *Proc. Int. Conf. on Learning Representations (ICLR)*, 2025.
- Difan Zou, Philip M Long, and Quanquan Gu. On the global convergence of training deep linear resnets. *arXiv preprint arXiv:2003.01094*, 2020.

A Additional related work

Scaling deep. Broadly speaking, our work is also related to mechanisms for scaling neural networks to greater depth. Normalization techniques are often believed to facilitate training at depth. For example, the normalization in pre-activation ResNets (He et al., 2016b) and transformers (Xiong et al., 2020) has been shown to improve training stability. Moreover, it is shown in (De and Smith, 2020) that batch normalization downscals the hidden activations on the residual branch by an order of square root of the network depth at initialization. Proper normalization techniques, in conjunction with residual connections, enable deeper LLMs (Wang et al., 2024a) and vision transformers (Touvron et al., 2021). At the same time, there are also works suggesting that normalization is not strictly necessary, as some of its early training benefits can be reproduced by carefully designed initialization; see e.g., (Zhang et al., 2019; De and Smith, 2020). Nevertheless, residual connections remain a central ingredient for modern deep neural networks.

Architecture-optimizer co-design. Recently, there has been a growing trend toward opening up the “black box” of neural networks and leverage learning dynamics to co-design architectures and optimizers for more efficient training. Much of this research focuses on LoRA (Hu et al., 2022) due to its structural simplicity. For instance, (Zhang et al., 2025; Wang et al., 2024b) investigate the gauge invariance underlying LoRA optimization, while (Lion et al., 2025) propose architectural redesigns to improve performance scaling relative to adapter rank. Furthermore, (Li et al., 2024) demonstrate that initialization can lead to an exponential gap in theoretically tractable settings. Our work aligns with this trajectory by demonstrating that residual connections significantly reshape the loss landscape.

B Missing proofs

This appendix offers the missing proofs for theories in the main paper. Our analysis leverages the following notations.

Additional notation. $\langle \cdot, \cdot \rangle_F$, $\text{Tr}(\cdot)$, $\text{rank}(\cdot)$ represent for Frobenius inner product, trace, and rank; $\lambda_i(\cdot)$ and $\sigma_i(\cdot)$ are the i -th largest eigenvalue and singular value. $\text{diag}(\mathbf{v})$ is the diagonal matrix whose diagonal entries are from vector \mathbf{v} , while $\text{diag}(\mathbf{M})$ refers to the vector formed by the diagonals of matrix \mathbf{M} . For simplicity, the subscripts of \mathcal{L}_1 and \mathcal{L}_2 are dropped when the objective is clearly specified.

B.1 Proof of Theorem 3.2

Before presenting the proof, we first simplify the optimization objective and look into the associated dynamics.

Recall that \mathbf{X} is orthogonal, so (2) can be equivalently rewritten as

$$\mathcal{L}(t) = \frac{1}{2} \left\| \mathbf{W}_3(t) \mathbf{W}_2(t) (\mathbf{W}_1(t) + \mathbf{I}_d) \mathbf{X} - \mathbf{Y} \right\|_F^2 = \frac{1}{2} \left\| \mathbf{W}_3(t) \mathbf{W}_2(t) (\mathbf{W}_1(t) + \mathbf{I}_d) - \mathbf{Y} \mathbf{X}^\top \right\|_F^2. \quad (9)$$

Defining $\mathbf{A} := \mathbf{Y} \mathbf{X}^\top$, the optimization dynamics then boil down to

$$\begin{aligned} \mathbf{E}(t) &= \mathbf{W}_3(t) \mathbf{W}_2(t) (\mathbf{W}_1(t) + \mathbf{I}_d) - \mathbf{A}, \\ \nabla_{\mathbf{W}_1} \mathcal{L}(t) &= \mathbf{W}_2(t)^\top \mathbf{W}_3^\top(t) \mathbf{E}(t), \\ \nabla_{\mathbf{W}_2} \mathcal{L}(t) &= \mathbf{W}_3(t)^\top \mathbf{E}(t) (\mathbf{W}_1^\top(t) + \mathbf{I}_d), \\ \nabla_{\mathbf{W}_3} \mathcal{L}(t) &= \mathbf{E}(t) (\mathbf{W}_1^\top(t) + \mathbf{I}_d) \mathbf{W}_2^\top(t). \end{aligned}$$

Given these, the gradient flow (1) can thus be written as

$$\frac{d\mathbf{W}_1(t)}{dt} = -\nabla_{\mathbf{W}_1} \mathcal{L}(t), \quad \frac{d\mathbf{W}_2(t)}{dt} = -\nabla_{\mathbf{W}_2} \mathcal{L}(t), \quad \frac{d\mathbf{W}_3(t)}{dt} = -\nabla_{\mathbf{W}_3} \mathcal{L}(t). \quad (10)$$

Theorem B.1 (Formal restatement of Theorem 3.2). *There exists a problem instance of (9) with diagonally initialized weights, such that if $\mathbf{W}_1[d, d](0) \in [-0.5, 0]$ and $\mathbf{W}_2[d, d](0) = \mathbf{W}_3[d, d](0) \in (0, 0.5]$, then gradient flow (10) can only converge sublinearly at*

$$\mathcal{L}(t) \geq \Omega(1/t^2).$$

Proof. We construct a specific instance of \mathbf{A} and analyze the resultant gradient flow dynamics. In particular, consider a diagonal matrix \mathbf{A} with rank $r_A < d$. That is, $\mathbf{A} = \text{diag}(\sigma_1, \sigma_2, \dots, \sigma_{r_A}, 0, \dots, 0)$, where the last singular value $\sigma_d = 0$. Furthermore, since $\mathbf{W}_1(0)$, $\mathbf{W}_2(0)$ and $\mathbf{W}_3(0)$ are diagonally initialized, it can be verified that the dynamics of gradient flow is diagonally separable throughout training. Specifically, letting $w_i(t)$, $u_i(t)$ and $v_i(t)$ be the i -th diagonal of $\mathbf{W}_1(t) + \mathbf{I}_d$, $\mathbf{W}_2(t)$ and $\mathbf{W}_3(t)$, the dynamics for $\forall i \in \{1, 2, \dots, d\}$ can be written in a decoupled and coordinate-wise form as

$$a_i(t) := w_i(t)u_i(t)v_i(t), \quad (11a)$$

$$\frac{dw_i(t)}{dt} = -u_i(t)v_i(t)(a_i(t) - \sigma_i), \quad (11b)$$

$$\frac{du_i(t)}{dt} = -w_i(t)v_i(t)(a_i(t) - \sigma_i), \quad (11c)$$

$$\frac{dv_i(t)}{dt} = -w_i(t)u_i(t)(a_i(t) - \sigma_i). \quad (11d)$$

We now focus on the coordinate $i = d$, for which $\sigma_d = 0$. Moreover, since we initialize $u_d(0) = v_d(0)$, Lemma B.2 leads to $u_d(t) = v_d(t)$ for $\forall t \geq 0$. Combining this with (11) we obtain

$$\begin{aligned} \frac{da_d(t)}{dt} &= u_d(t)v_d(t)\frac{dw_d(t)}{dt} + w_d(t)v_d(t)\frac{du_d(t)}{dt} + w_d(t)u_d(t)\frac{dv_d(t)}{dt} \\ &= -u_d^4(t)a_d(t) - 2w_d^2(t)u_d^2(t)a_d(t) \\ &= -\frac{a_d^3(t)}{w_d^2(t)} - 2w_d(t)a_d^2(t). \end{aligned}$$

Moreover, the initialization yields $w_d(0) = 1 + \mathbf{W}_1[d, d](0) \in [0.5, 1]$ and $u_d(0) = v_d(0) \in (0, 0.5]$. It then follows from Lemma B.4 that $0 \leq u_d(t) = v_d(t) \leq w_d(t) \leq 1$.

Therefore, it holds

$$a_d(t) = w_d(t)u_d(t)v_d(t) = w_d(t)u_d^2(t) \in [0, 1].$$

Using this, we can further obtain

$$\begin{aligned} \frac{da_d(t)}{dt} &= -\frac{a_d^3(t)}{w_d^2(t)} - 2w_d(t)a_d^2(t) \\ &\stackrel{(a)}{\geq} -\frac{a_d^3(t)}{w_d^2(t)} - 2a_d^2(t) \\ &\stackrel{(b)}{\geq} -a_d^{7/3}(t) - 2a_d^2(t) \\ &\stackrel{(c)}{\geq} -3a_d^2(t) \end{aligned}$$

where (a) is by Lemmas B.4; (b) utilizes Lemma B.5 with $a_d(t) > 0$; and (c) follows from $a_d(t) \leq 1$.

The inequality above implies that $a_d(t) \geq \frac{a_d(0)}{1+3a_d(0)t}$ as a result of Lemma B.12. Hence, we arrive at

$$\mathcal{L}(t) = \frac{1}{2} \sum_{i=1}^d (a_i(t) - \sigma_i)^2 \geq \frac{1}{2} (a_d(t))^2 \geq \frac{a_d^2(0)}{(1+3a_d(0)t)^2} = \Omega(1/t^2)$$

where $a_d(0) = w_d(0)u_d^2(0) > 0$. The proof is thus completed. \square

Lemma B.2. *If $u_d(0) = v_d(0)$, then $u_d(t) = v_d(t)$, $\forall t \geq 0$.*

Proof. This symmetry follows immediately from the observation that $\frac{du_d(t)}{dt} = \frac{dv_d(t)}{dt}$ whenever $u_d(t) = v_d(t)$. As $u_d(0) = v_d(0)$, this symmetry always holds throughout the optimization. \square

Lemma B.3. *Under gradient flow (10), it holds that*

$$\frac{da_d^2(t)}{dt} \leq 0.$$

Proof. It is straightforward to see that

$$\begin{aligned} \frac{1}{2} \frac{da_d^2(t)}{dt} &= a_d(t)u_d(t)v_d(t) \frac{dw_i(t)}{dt} + a_d(t)w_d(t)v_d(t) \frac{du_d(t)}{dt} + w_d(t)u_d(t)a_d(t) \frac{dv_d(t)}{dt} \\ &= -u_d^4(t)a_d^2(t) - 2w_d^2(t)u_d^2(t)a_d^2(t) \leq 0 \end{aligned}$$

where we used $u_d(t) = v_d(t)$ given by Lemma B.2, together with the dynamics in (11). \square

Lemma B.4. *If $0 < u_d(0) = v_d(0) \leq w_d(0) \leq 1$, then $0 \leq u_d(t) = v_d(t) \leq w_d(t) \leq 1$.*

Proof. Leveraging (11) and Lemma B.2, it can be readily verified that

$$\frac{dw_d^2(t)}{dt} = \frac{du_d^2(t)}{dt} = -2w_d(t)u_d(t)v_d(t)a_d(t) = -2a_d^2(t) \leq 0.$$

This implies

$$w_d^2(t) - w_d^2(0) = u_d^2(t) - u_d^2(0) := \Delta(t) \leq 0,$$

which proves $w_d^2(t) \geq u_d^2(t)$ as $w_d(0) \geq u_d(0) > 0$.

Note that

$$\left| \frac{dw_d(t)}{dt} \right| = u_d^2(t)|a_d(t)| = u_d^4(t)|w_d(t)| \leq u_d^4(0)|w_d(0)| \leq 1.$$

This suggests $w_d(t)$ is a polynomial ODE that is locally Lipschitz, it has no jump according to Picard–Lindelöf theorem. As $w_d(0) \in (0, 1]$ and $w_d^2(t)$ is non-increasing, we must have $0 \leq w_d(t) \leq w_d(0) \leq 1$. Likewise, it also holds $0 \leq u_d(t) \leq u_d(0) < 1$.

Combining these results, we conclude that $0 \leq u_d(t) = v_d(t) \leq w_d(t) \leq 1$, which completes the proof. \square

Lemma B.5. *If $0 < u_d(0) = v_d(0) \leq w_d(0) \leq 1$, then $w(t) \geq a_d^{1/3}(t)$.*

Proof. It directly follows from Lemmas B.2 and B.4 that

$$a_d^2(t) = u_d^4(t)w_d^2(t) \leq w_d^6(t).$$

Given that $w_d(t) \geq 0$ by Lemma B.4, we reach at $w_d(t) \geq a_d^{1/3}(t)$. \square

B.2 Proof of Theorem 3.3

Similar to (9), the objective (4) can be simplified as

$$\mathcal{L}(t) = \frac{1}{2} \left\| \mathbf{W}_3(t)(\mathbf{W}_2(t)\mathbf{W}_1(t) + \mathbf{I}_d)\mathbf{X} - \mathbf{Y} \right\|_{\text{F}}^2 = \frac{1}{2} \left\| \mathbf{W}_3(t)(\mathbf{W}_2(t)\mathbf{W}_1(t) + \mathbf{I}_d) - \mathbf{A} \right\|_{\text{F}}^2. \quad (12)$$

The associated optimization dynamics are

$$\mathbf{E}(t) := \mathbf{W}_3(t)(\mathbf{W}_2(t)\mathbf{W}_1(t) + \mathbf{I}_d) - \mathbf{A}, \quad (13a)$$

$$\nabla_{\mathbf{W}_1} \mathcal{L}(t) = \mathbf{W}_2(t)^T \mathbf{W}_3^T(t) \mathbf{E}(t), \quad (13b)$$

$$\nabla_{\mathbf{W}_2} \mathcal{L}(t) = \mathbf{W}_3(t)^T \mathbf{E}(t) \mathbf{W}_1^T(t), \quad (13c)$$

$$\nabla_{\mathbf{W}_3} \mathcal{L}(t) = \mathbf{E}(t)(\mathbf{W}_2(t)\mathbf{W}_1(t) + \mathbf{I}_d)^T. \quad (13d)$$

And the gradient flow is the same as (10).

Theorem B.6 (Formal restatement of Theorem 3.3). *If $\|\mathbf{W}_i(0)\|_{\text{F}} \leq \delta := \sqrt{\frac{\lambda}{2}} \exp\{-\frac{\sqrt{\lambda \mathcal{L}(0)}}{(1-\lambda)^2} - \frac{\sqrt{2\pi \mathcal{L}(0)}}{2(1-\lambda)^3}\}$, $i = 1, 2, 3$ for some $\lambda \in (0, 1)$, then gradient flow (10) achieves linear convergence*

$$\mathcal{L}(t) \leq \mathcal{L}(0)e^{-2(1-\lambda)^2 t}.$$

Proof. Recall from the last subsection that the ODEs involved are polynomial and locally Lipschitz, and thus have no jump. Then we can define $T := \min\{t \geq 0 \mid \|\mathbf{W}_1(t)\mathbf{W}_2(t)\| \geq \lambda\}$ to be the first time satisfying $\|\mathbf{W}_1\mathbf{W}_2\| \geq \lambda$. Applying Lemma B.8, it follows that

$$\mathcal{L}(t) \leq \mathcal{L}(0)e^{-2(1-\lambda)^2 t}, \quad \forall t \leq T.$$

Next applying Lemma B.11, we acquire for all $t \leq T$ that

$$\begin{aligned} \|\mathbf{W}_1(t)\mathbf{W}_2(t)\|_2 &\leq \|\mathbf{W}_1(t)\|_{\text{F}} \|\mathbf{W}_2(t)\|_{\text{F}} \leq \frac{1}{2} \left(\|\mathbf{W}_1(t)\|_{\text{F}}^2 + \|\mathbf{W}_2(t)\|_{\text{F}}^2 \right) \\ &\leq \frac{1}{2} \left(\|\mathbf{W}_1(0)\|_{\text{F}}^2 + \|\mathbf{W}_2(0)\|_{\text{F}}^2 \right) \exp \left\{ \frac{2\delta\sqrt{2\mathcal{L}(0)}}{(1-\lambda)^2} + \frac{\sqrt{2\pi\mathcal{L}(0)}}{(1-\lambda)^3} \right\} \\ &\leq \delta^2 \exp \left\{ \frac{2\delta\sqrt{2\mathcal{L}(0)}}{(1-\lambda)^2} + \frac{\sqrt{2\pi\mathcal{L}(0)}}{(1-\lambda)^3} \right\} \\ &= \frac{\lambda}{2} \exp \left\{ \frac{2\sqrt{2\mathcal{L}(0)}}{(1-\lambda)^2} \left(\delta - \sqrt{\frac{\lambda}{2}} \right) \right\} \\ &\stackrel{(a)}{\leq} \frac{\lambda}{2} < \lambda \end{aligned}$$

where (a) is due to $\delta = \sqrt{\frac{\lambda}{2}} \exp\{-\frac{\sqrt{2\mathcal{L}(0)}}{(1-\lambda)^2} - \frac{\sqrt{2\pi\mathcal{L}(0)}}{2(1-\lambda)^3}\} \leq \sqrt{\frac{\lambda}{2}}$. As $\|\mathbf{W}_1(t)\mathbf{W}_2(t)\|_2$ has no jump, this indicates our choice of δ and λ ensures $\|\mathbf{W}_1(t)\mathbf{W}_2(t)\|_2 < \lambda$ always holds; that is, $T = +\infty$. \square

Lemma B.7. *Under gradient flow (10), we have that*

$$\frac{d\mathcal{L}}{dt} = -\sum_{i=1}^3 \|\nabla_{\mathbf{W}_i} \mathcal{L}(t)\|_F^2 \leq 0.$$

Proof. It is straightforward to see that

$$\begin{aligned} \frac{d\mathcal{L}}{dt} &= \left\langle \nabla_{\mathbf{W}_1} \mathcal{L}(t), \frac{d\mathbf{W}_1}{dt} \right\rangle + \left\langle \nabla_{\mathbf{W}_2} \mathcal{L}(t), \frac{d\mathbf{W}_2}{dt} \right\rangle + \left\langle \nabla_{\mathbf{W}_3} \mathcal{L}(t), \frac{d\mathbf{W}_3}{dt} \right\rangle \\ &= -\|\nabla_{\mathbf{W}_1} \mathcal{L}(t)\|_F^2 - \|\nabla_{\mathbf{W}_2} \mathcal{L}(t)\|_F^2 - \|\nabla_{\mathbf{W}_3} \mathcal{L}(t)\|_F^2 \leq 0. \end{aligned}$$

This concludes the proof. \square

Lemma B.8. *For $\lambda \in (0, 1)$, defining $T := \min\{t \geq 0 \mid \|\mathbf{W}_1(t)\mathbf{W}_2(t)\| \geq \lambda\}$, then the loss converges linearly at*

$$\mathcal{L}(t) \leq \mathcal{L}(0)e^{-2(1-\lambda)^2 t}, \quad t \leq T.$$

Proof. We start with bounding

$$\|\nabla_{\mathbf{W}_3} \mathcal{L}(t)\|_F^2 \stackrel{(a)}{\geq} \|\mathbf{E}(t)\|_F^2 \sigma_d^2(\mathbf{I}_d + \mathbf{W}_2(t)\mathbf{W}_1(t)) \stackrel{(b)}{\geq} (1-\lambda)^2 \|\mathbf{E}(t)\|_F^2$$

where (a) is by Lemma B.13; and (b) comes from $\sigma_d(\mathbf{I}_d + \mathbf{W}_1(t)\mathbf{W}_2(t)) \geq 1 - \|\mathbf{W}_1(t)\mathbf{W}_2(t)\| \geq 1 - \lambda$ when $t \leq T$.

Now based on Lemma B.7, it follows that

$$\frac{d\mathcal{L}}{dt} = -\sum_{i=1}^3 \|\nabla_{\mathbf{W}_i} \mathcal{L}\|_F^2 \leq -\|\nabla_{\mathbf{W}_3} \mathcal{L}\|_F^2 \leq -(1-\lambda)^2 \|\mathbf{E}(t)\|_F^2 = -2(1-\lambda)^2 \mathcal{L}(t).$$

This directly results in $\mathcal{L}(t) \leq \mathcal{L}(0)e^{-2(1-\lambda)^2 t}$. \square

Lemma B.9. *Under gradient flow (10), it holds that*

$$\|\mathbf{W}_3(t)\|_F \leq \|\mathbf{W}_3(0)\|_F + \sqrt{t\mathcal{L}(0)}.$$

Proof. From the gradient flow, it can be seen that

$$\mathbf{W}_3(t) = \mathbf{W}_3(0) - \int_0^t \nabla_{\mathbf{W}_3} \mathcal{L}(s) ds.$$

Further taking norm on both sides, we have that

$$\begin{aligned}
\|\mathbf{W}_3(t)\|_{\text{F}} &\leq \|\mathbf{W}_3(0)\|_{\text{F}} + \left\| \int_0^t \nabla_{\mathbf{W}_3} \mathcal{L}(s) \mathbf{d}s \right\| \\
&\leq \|\mathbf{W}_3(0)\|_{\text{F}} + \int_0^t 1 \times \|\nabla_{\mathbf{W}_3} \mathcal{L}(s)\|_{\text{F}} \mathbf{d}s \\
&\stackrel{(a)}{\leq} \|\mathbf{W}_3(0)\|_{\text{F}} + \sqrt{t \int_0^t \|\nabla_{\mathbf{W}_3} \mathcal{L}(s)\|_{\text{F}}^2 \mathbf{d}s} \\
&\leq \|\mathbf{W}_3(0)\|_{\text{F}} + \sqrt{t \int_0^t \sum_{i=1}^3 \|\nabla_{\mathbf{W}_i} \mathcal{L}(s)\|_{\text{F}}^2 \mathbf{d}s} \\
&\stackrel{(b)}{=} \|\mathbf{W}_3(0)\|_{\text{F}} + \sqrt{t(\mathcal{L}(0) - \mathcal{L}(t))} \\
&\stackrel{(c)}{\leq} \|\mathbf{W}_3(0)\|_{\text{F}} + \sqrt{t\mathcal{L}(0)}
\end{aligned}$$

where (a) comes from Cauchy–Schwarz inequality; (b) uses Lemma B.7; (c) is because the loss is always greater than 0. \square

Lemma B.10. *Under gradient flow (10), it follows that*

$$\frac{d\|\mathbf{W}_1(t)\|_{\text{F}}^2}{dt} = \frac{d\|\mathbf{W}_2(t)\|_{\text{F}}^2}{dt}.$$

Proof. Note that

$$\frac{d\|\mathbf{W}_1(t)\|_{\text{F}}^2}{dt} = 2 \left\langle \mathbf{W}_1, \frac{d\mathbf{W}_1(t)}{dt} \right\rangle = -2 \text{Tr}(\mathbf{W}_1^\top(t) \mathbf{W}_2^\top(t) \mathbf{W}_3^\top(t) \mathbf{E}(t)).$$

Similarly, we have

$$\begin{aligned}
\frac{d\|\mathbf{W}_2(t)\|_{\text{F}}^2}{dt} &= 2 \left\langle \mathbf{W}_2, \frac{d\mathbf{W}_2(t)}{dt} \right\rangle = -2 \text{Tr}(\mathbf{W}_2^\top(t) \mathbf{W}_3^\top(t) \mathbf{E}(t) \mathbf{W}_1^\top(t)) \\
&= -2 \text{Tr}(\mathbf{W}_1^\top(t) \mathbf{W}_2^\top(t) \mathbf{W}_3^\top(t) \mathbf{E}(t)).
\end{aligned}$$

The proof is thus completed. \square

Lemma B.11. *When $t \leq T$, it holds that*

$$\|\mathbf{W}_1(t)\|_{\text{F}}^2 + \|\mathbf{W}_2(t)\|_{\text{F}}^2 \leq \left(\|\mathbf{W}_1(0)\|_{\text{F}}^2 + \|\mathbf{W}_2(0)\|_{\text{F}}^2 \right) e^M$$

where M is given by

$$M := \frac{2\sqrt{2\mathcal{L}(0)}\|\mathbf{W}_3(0)\|_{\text{F}}}{(1-\lambda)^2} + \frac{\sqrt{2\pi}\mathcal{L}(0)}{(1-\lambda)^3}.$$

Proof. Using Lemma B.10, we obtain

$$\begin{aligned}
\frac{d\|\mathbf{W}_1\|_F^2 + \|\mathbf{W}_2\|_F^2}{dt} &= -4\text{Tr}(\mathbf{W}_1^\top(t)\mathbf{W}_2^\top(t)\mathbf{W}_3^\top(t)\mathbf{E}(t)) \\
&\leq 4\|\mathbf{W}_1(t)\|_F\|\mathbf{W}_2(t)\|_F\|\mathbf{W}_3(t)\|_F\|\mathbf{E}(t)\|_F \\
&\leq 2\|\mathbf{W}_3(t)\|_F\|\mathbf{E}(t)\|_F \cdot \left(\|\mathbf{W}_1(t)\|_F^2 + \|\mathbf{W}_2(t)\|_F^2\right) \\
&\stackrel{(a)}{\leq} 2\|\mathbf{W}_3(t)\|_F\sqrt{2\mathcal{L}(0)}e^{-(1-\lambda)^2t} \cdot \left(\|\mathbf{W}_1(t)\|_F^2 + \|\mathbf{W}_2(t)\|_F^2\right) \\
&\stackrel{(b)}{\leq} 2\left(\|\mathbf{W}_3(0)\|_F + \sqrt{t\mathcal{L}(0)}\right) \cdot \sqrt{2\mathcal{L}(0)}e^{-(1-\lambda)^2t} \cdot \left(\|\mathbf{W}_1(t)\|_F^2 + \|\mathbf{W}_2(t)\|_F^2\right)
\end{aligned}$$

where (a) comes from Lemma B.8, which shows that $\mathcal{L}(t) = \frac{1}{2}\|\mathbf{E}(t)\|_F^2 \leq \mathcal{L}(0)e^{-2(1-\lambda)^2t}$; and (b) is by Lemma B.9.

Now applying Lemma B.14, with $c_1 = 2\sqrt{2\mathcal{L}(0)}\|\mathbf{W}_3(0)\|_F$, $c_2 = 2\sqrt{2\mathcal{L}(0)}$ and $c_3 = (1-\lambda)^2$, and $x(t) = \|\mathbf{W}_1(t)\|_F^2 + \|\mathbf{W}_2(t)\|_F^2$, we obtain for $\forall t \leq T$ that

$$\|\mathbf{W}_1(t)\|_F^2 + \|\mathbf{W}_2(t)\|_F^2 \leq \left(\|\mathbf{W}_1(0)\|_F^2 + \|\mathbf{W}_2(0)\|_F^2\right)e^M, \quad M = \frac{2\sqrt{2\mathcal{L}(0)}\|\mathbf{W}_3(0)\|_F}{(1-\lambda)^2} + \frac{\sqrt{2\pi\mathcal{L}(0)}}{(1-\lambda)^3}.$$

The proof is thus completed. \square

B.3 Additional auxiliary lemmas

This subsection provides useful lemmas for proving our main results.

Lemma B.12. *If $\frac{da(t)}{dt} \geq -3a^2(t)$, it holds that $a(t) \geq \frac{a(0)}{1+3a(0)t}$.*

Proof. We can rewrite $\frac{da(t)}{dt} \geq -3a^2(t)$ as

$$\frac{1}{a^2(t)} \frac{da(t)}{dt} \geq -3.$$

Integrating both sides renders

$$-\frac{1}{a(s)} \Big|_0^t \geq -3t$$

which concludes the proof. \square

Lemma B.13. *Given two matrices $\mathbf{A} \in \mathbb{R}^{r \times r}$ and $\mathbf{B} \in \mathbb{R}^{r \times r}$, it holds that $\|\mathbf{AB}\|_F \geq \sigma_r(\mathbf{A})\|\mathbf{B}\|_F^2$.*

Proof. Let \mathbf{b}_i be the i th column of \mathbf{B} . It then follows that

$$\begin{aligned}
\|\mathbf{AB}\|_F^2 &= \sum_{i=1}^r \|\mathbf{Ab}_i\|_2^2 = \sum_{i=1}^r \left\| \mathbf{A} \frac{\mathbf{b}_i}{\|\mathbf{b}_i\|} \right\|_2^2 \|\mathbf{b}_i\|_2^2 \\
&\geq \min_{\|\mathbf{u}\|=1} \|\mathbf{Au}\|^2 \sum_{i=1}^r \|\mathbf{b}_i\|_2^2 = \sigma_r^2(\mathbf{A})\|\mathbf{B}\|_F^2.
\end{aligned}$$

The proof is thus completed. \square

Lemma B.14. *If $x(t) \geq 0$, $\forall t \leq T$, and it holds for constant $c_1 \geq 0, c_2 \geq 0, c_3 > 0$ that*

$$\frac{dx}{dt} \leq (c_1 + c_2\sqrt{t})e^{-c_3t}x(t), \quad \forall t \leq T,$$

then we have

$$x(t) \leq x(0)e^M, \quad \forall t \leq T$$

where $M := \frac{c_1}{c_3} + \frac{\sqrt{\pi}}{2}c_2c_3^{-3/2}$.

Proof. To start with, since $x(t) > 0$, $\forall t \leq T$, it follows

$$\frac{d \ln x(t)}{dt} = \frac{1}{x(t)} \frac{dx(t)}{dt} \leq (c_1 + c_2\sqrt{t})e^{-c_3t}.$$

Integrating both sides, we acquire

$$\begin{aligned} \ln x(t) - \ln x(0) &\leq \int_0^t (c_1 + c_2\sqrt{s})e^{-c_3s} ds \\ &\leq \int_0^\infty (c_1 + c_2\sqrt{s})e^{-c_3s} ds \\ &\leq \frac{c_1}{c_3} + c_2 \int_0^\infty \sqrt{s}e^{-c_3s} ds. \end{aligned}$$

Next, notice that

$$\int_0^\infty \sqrt{s}e^{-c_3s} ds \stackrel{(a)}{=} \frac{1}{c_3^{3/2}} \int_0^\infty \sqrt{u}e^{-u} du \stackrel{(b)}{=} \frac{1}{c_3^{3/2}} \Gamma\left(\frac{3}{2}\right) \stackrel{(c)}{=} c_3^{-3/2} \frac{1}{2} \Gamma\left(\frac{1}{2}\right) = \frac{\sqrt{\pi}}{2} c_3^{-3/2}$$

where (a) is by change of variable $u = c_3s$; (b) uses the definition of Gamma function $\Gamma(z) = \int_0^\infty t^{z-1}e^{-t} dt$; and (c) relies on $\Gamma(z+1) = z\Gamma(z)$ and $\Gamma(1/2) = \sqrt{\pi}$.

Combining these together offers

$$\ln x(t) - \ln x(0) \leq \frac{c_1}{c_3} + \frac{\sqrt{\pi}}{2} c_2 c_3^{-3/2} := M.$$

The proof is thus completed. \square

B.4 Extension to more than 3 layers

The proof for LLNs of more than 3 layers follows the same strategy as the proceeding two theorems. To avoid redundancy, we provide a proof sketch and omit the step-by-step details.

For the slow-convergence case (i.e., K -layer LNN with the 0:1 shortcut), one can construct a diagonal initialization with $\mathbf{W}_1[d, d](0) \in [-0.5, 0]$, and $\mathbf{W}_2[d, d](0) = \dots = \mathbf{W}_K[d, d](0) \in (0, 0.5]$, and likewise a rank-deficient diagonal matrix \mathbf{A} . By following the dynamic analysis in Lemma B.2, it can be shown that $\mathbf{W}_2[d, d](t) = \dots = \mathbf{W}_K[d, d](t)$, $\forall t \geq 0$. As a consequence, Lemma B.4 can be extended to establish that $0 \leq \mathbf{W}_2[d, d](t) = \dots = \mathbf{W}_K[d, d](t) \leq 1 + \mathbf{W}_1[d, d](t) \leq 1$, $\forall t \geq 0$. To this end, applying the same arguments as in the proof of Theorem B.1 to the dynamics of $a_d(t) := (1 + \mathbf{W}_1[d, d](t)) \prod_{k=2}^K \mathbf{W}_k[d, d](t)$ yields the sublinear convergence.

In contrast, K -layer LNN with the $0:K-1$ shortcut can be shown to always converge linearly. The core idea is to replace the term $\|\mathbf{W}_1(t)\mathbf{W}_2(t)\|$ in the original proof with the more generic $\|\prod_{k=1}^{K-1} \mathbf{W}_k(t)\|$, and to generalize $\|\mathbf{W}_3\|_F$ in Lemma B.9 to $\|\mathbf{W}_K\|_F$. Accordingly, Lemma B.10 is extended to

$$\frac{d\|\mathbf{W}_1(t)\|_F^2}{dt} = \dots = \frac{d\|\mathbf{W}_{K-1}(t)\|_F^2}{dt}.$$

Finally, with the same steps in the proof of Theorem B.6, linear convergence then follows directly upon choosing an appropriate δ .

C Experimental setups

This appendix offers the detailed setups for reproducing the results reported in the main paper. All our codes are written in python. The LLM pretraining and RL tests are performed on a computing node with $4 \times$ A100 GPUs, while the diffusion models are trained on $2 \times$ H100 GPUs.

C.1 Datasets

In the following, we provide a brief introduction to the datasets used in our tests.

Colossal Clean Crawled Corpus (C4) ([Raffel et al., 2020](#)) is a large-scale English text dataset derived from the April 2019 Common Crawl snapshot consisting of cleaned web text. It was introduced as part of the development of Google’s T5 model ([Raffel et al., 2020](#)), and has been widely used as a standard pretraining corpus for LLMs due to its scale, diversity, and high quality. The dataset is available online from TensorFlow datasets².

ImageNet-1K ([Krizhevsky et al., 2012](#)) is a large-scale image classification dataset containing approximately 1.28 million training images and 50,000 validation images annotated across 1,000 object categories. The dataset is a subset of the full ImageNet (ILSVRC-12) and is organized according to the WordNet hierarchy, with images collected from the web and manually labeled. ImageNet-1K has become a standard benchmark for training and evaluating visual recognition models, particularly in large-scale image classification and representation learning. The dataset is available online³ for non-commercial research and/or educational purposes.

C.2 Models

Next, we elaborate the models adopted in our evaluation.

LLaMA ([Touvron et al., 2023](#)) is a family of decoder-only transformer-based large language models introduced by Meta. In this work, LLaMA is implemented using the Hugging Face `transformers` library, following the official architecture definition⁴.

Diffusion Transformer (DiT) ([Peebles and Xie, 2023](#)) is a generative image model that replaces conventional convolutional U-Nets in diffusion models with a vision transformer operating on image patches. Reference implementations of DiT are publicly available⁵ and released under the CC-BY-NC license.

²<https://www.tensorflow.org/datasets/catalog/c4>

³<https://image-net.org>

⁴https://github.com/huggingface/transformers/blob/main/src/transformers/models/llama/modeling_llama.py

⁵<https://github.com/facebookresearch/DiT>

Table 7 Hyperparameters for pre-training LLMs.

Hyperparameter	FullPT(+ANCRe)			1B	60M	GaLore(+ANCRe)		
	60M	130M	350M			130M	350M	1B
Max seq. len.				256				
Learning rate	5×10^{-3}	1×10^{-3}	1×10^{-3}	5×10^{-4}	1×10^{-2}	5×10^{-2}	5×10^{-2}	5×10^{-3}
Training steps	10K	20K	60K	100K	10K	20K	60K	100K
Warmup steps	1K	2K	6K	10K	1K	2K	6K	10K
Global batch size				512				
Micro Batch size	256	128	64	16	256	128	64	16
GPUs	1×A100	1×A100	4×A100	2×H100	1×A100	1×A100	4×A100	2×H100

Table 8 ANCRe temperature τ for RL tests.

Environment	ResNet-16	ResNet-64
Humanoid	0.01	0.01
Ant Big Maze	0.01	0.01
Arm Push Hard	0.1	0.1
Arm Binpick Hard	0.01	0.1

Residual Networks (ResNets) (He et al., 2016a) are a class of deep convolutional neural networks, characterized by residual connections that enable the effective training of very deep architectures. ResNets have become a foundational backbone for a wide range of tasks. Standard ResNet implementations⁶ are released under permissive MIT license. Our test relies on the variants used in (Wang et al., 2025), where cascaded shortcuts are added to every block of four layers.

C.3 Hyperparameters

We next list the hyperparameters for running the experiments.

Pre-training of LLaMAs. The experimental setup follows (Lialin et al., 2024; Zhao et al., 2024), with all hyperparameters except the learning rate fixed to their default values. We use the AdamW optimizer (Loshchilov and Hutter, 2017) with gradient accumulation. The learning rate is tuned over $\{5 \times 10^{-4}, 1 \times 10^{-3}, 5 \times 10^{-3}, 1 \times 10^{-2}, 5 \times 10^{-2}\}$; see Table 7 for further details. For GaLore, the rank, update projection gap, and scaling factor are set to their default values of 128, 200, and 0.25, respectively. For ANCRe, the softmax temperature τ in (8) is fixed to 0.01 without additional tuning.

Pre-training of DiTs. The experimental settings are from (Peebles and Xie, 2023) without any modifications, including the learning rate. Specifically, we use images of size 256×256 , a global batch size of 256, a learning rate of 1×10^{-4} , a patch size of 2×2 , and train for 80 epochs (i.e., 400K iterations) using BF16 precision. The ANCRe temperature is set to $\tau = 0.1$ for both DiT-S/2 and DiT-B/2. All experiments are conducted on two H100 GPUs.

RL with ResNets. The numerical experiments follow the experimental setup of (Wang et al., 2025). Specifically, the episode length is set to 1000, and training is conducted for 100M environment steps. The number of training epochs and the batch size are 100 and 512, respectively, with 512 parallel environments. The learning rate is fixed at 3×10^{-4} . Both the actor and critic networks use a

⁶<https://github.com/KaimingHe/deep-residual-networks>

hidden dimension of 256, while the network width is selected from $\{16, 64\}$. For ANCRe, the softmax temperature τ is coarsely tuned from $\{10^{-3}, 10^{-2}, 10^{-1}\}$, which can be found in Table 8.